Title

Tailoring Piezoresistive Sensitivity of Multilayer Carbon Nanotube Composite Strain Sensors

Journal

Journal of Intelligent Material Systems and Structures, 19(7)

ISSN

1045-389X

Authors

Loh, KJ
Lynch, JP
Shim, BS
et al.

Publication Date

2008-07-01

DOI

10.1177/1045389x07079872

Peer reviewed

Tailoring Piezoresistive Sensitivity of Multilayer Carbon Nanotube Composite Strain Sensors

K. J. LOH[1], J. P. LYNCH*[1,2], B. S. SHIM[3], AND N. A. KOTOV[3]

[1]*Department of Civil & Environmental Engineering, University of Michigan, Ann Arbor, MI 48109, USA*
[2]*Department of Electrical Engineering & Computer Science, University of Michigan, Ann Arbor, MI 48109, USA*
[3]*Department of Chemical Engineering, University of Michigan, Ann Arbor, MI 48109, USA*

ABSTRACT: In recent years, carbon nanotubes have been utilized for a variety of applications including nanoelectronics and various types of sensors. In particular, researchers have sought to take advantage of the superior electrical properties of carbon nanotubes for fabricating novel strain sensors. This paper presents a single-walled carbon nanotube (SWNT)-polyelectrolyte (PE) composite thin film strain sensor fabricated with a layer-by-layer (LbL) process. Optimization of bulk SWNT-PE strain sensor properties is achieved by varying various LbL fabrication parameters followed by characterization of strain sensing electromechanical responses. An RC-circuit model is proposed and validated with electrical impedance spectroscopy to fit experimental results and to identify equivalent circuit element parameters sensitive to strain. Experimental results suggest consistent trends between SWNT and PE concentrations to strain sensor sensitivities. Simply by adjusting the weight fraction of SWNT solutions and film thickness, strain sensitivities between 0.1 and 1.8 have been achieved. While SWNT-PE strain sensitivity is lower than traditional metal-foil strain gauges (2.1), the LbL method allows for precise tailoring of the properties (*i.e.* strain sensitivity, resistivity, among others) of a high capacity (±10,000 μm/m) homogeneous multilayer strain sensor.

Key Words: carbon nanotube composite, electrical impedance spectroscopy, layer-by-layer, nanotechnology, strain sensor

* Corresponding author: jerlynch@umich.edu.

INTRODUCTION

Since the discovery of carbon nanotubes by Iijima in 1991 (Iijima, 1991), researchers have illustrated their functionality for a wide variety of applications including high-strength structural composites (Andrews *et al*., 1999), nanoelectronics (Tsukagoshi *et al*., 2002), various types of sensors (Kong *et al*., 2000; Wood *et al.*, 2000), among many others (Baughman *et al*., 2002). The widespread interest in adopting carbon nanotubes for novel applications owes to carbon nanotubes' spectacular mechanical (Salvetat *et al.*, 1999) and electrical properties (Baughman *et al*., 2002). Mechanically, the Young's modulus and ultimate tensile strength of single-walled carbon nanotubes (SWNTs) have been measured to be approximately $E \approx 1{,}054$ GPa and $\sigma_f \approx 75$ GPa, respectively, and for multi-walled carbon nanotubes (MWNTs) $E \approx 1{,}200$ GPa and $\sigma_f \approx 150$ GPa, respectively (Meyyappan, 2005). On the other hand, carbon nanotubes' high electrical conductivity stems from their nearly one-dimensional structure, thus approaching near-ballistic transport-type electronic behavior (Baughman *et al*., 2002).

Having realized the impressive mechanical and electrical properties of carbon nanotubes, researchers have undertaken the challenge to develop carbon nanotube-based sensors (Dai, 2002) in hopes to outperform the current generation of microelectromechanical systems' (MEMS) sensors. As opposed to the "top-down" MEMS sensor design paradigm, researchers can undertake a "bottom-up" approach to tailor macro-scale sensor properties at the atomistic length-scale. Among the various types of sensing transducers that exist, strain sensors are

particularly important for measuring component level strain in the laboratory and field environments for a variety of applications (Stein, 2006). Since direct strain measurements from a structural component can be correlated to induced localized stress fields, typically, a dense instrumentation is required to capture a two-dimensional stress field. However, due to the extensive cabling required for current popular strain sensors such as metal-foil strain gauges and fiber optic Bragg gratings, dense instrumentation may not be possible. As a result, many researchers over the past decade have proposed passive wireless strain sensors, also known as radio frequency identification (RFID)-based sensors, to eliminate the need for cables and collocated power sources, thereby opening the possibility of densely instrumented embedded monitoring systems (Mita and Takahira, 2002, 2003, 2004; Todd, 2005; Jia and Sun, 2006; Loh *et al.*, 2007b). Consequently, the objective of our current research is to fabricate a miniature cable-free thin film passive wireless strain sensor capable of being embedded within structural materials (for example, reinforced-concrete, among others). By using a layer-by-layer (LbL) self-assembly method, different components (*e.g.* sensor, antenna, etc.) of the wireless sensor can be fabricated in a single thin film structure using one fabrication methodology. Integral to an RFID-based strain sensor is the piezoresistive element; this element changes resistance in linear proportion to applied strain. In this study, piezoresistive properties are encoded in LbL thin films by utilizing carbon nanotubes and polyelectrolyte species to yield a homogeneous composite multilayer film structure.

Early experimental investigations of carbon nanotubes as mechanical sensors have been presented by Peng *et al.* (2001). These researchers have sought to identify changes in the electrical-mechanical properties of SWNTs suspended over patterned silicon oxide/silicon substrate trenches while the nanotubes are manipulated by an atomic force microscope (AFM) tip. Their results indicate promise for strain sensing as they have identified decreasing conductance up to two orders of magnitude of individual carbon nanotubes as AFM tips bend them (Peng *et al.*, 2001; Minot *et al.*, 2003; Tombler *et al.*, 2000). Similar numerical results using computed DFT-UFF (density-functional theory-universal force field) calculations have also indicated similar trends (Maiti *et al.*, 2002). Instead of manipulating individual SWNTs, Dharap *et al.* (2004) have used carbon nanotube films, called "buckypaper," and discovered linear changes in voltage as the buckypaper specimen is strained in low tension-compression cycles ($\varepsilon < \pm 400\ \mu m/m$). Continued work by Li *et al.* (2004) have shown that Raman wavenumber shifts of the G band of carbon nanotube films indicate that the nanotubes' electrical properties are altered as they are strained. Furthermore, Lanzara and Cheng (2004) utilize an aligned multi-walled carbon nanotube nano-electrode-array (MWNT-NEA) embedded in a polymer matrix to detect nano-scale strain deformations. The fabricated MWNT-NEA strain sensors could capture strains up to $\varepsilon = 0.78$ while maintaining linear response properties. Similar to Dharap *et al.* (2004), Kang *et al.* (2006) has developed a SWNT-polymer composite buckypaper exhibiting linear piezoresistivity up to $\varepsilon < 500\ \mu m/m$. Their work is extended to employ MWNTs to fabricate long films for a continuous neuron sensor.

Although many carbon nanotube-based strain transducers have been proposed, few have developed a scheme to control LbL fabrication parameters to yield desired strain sensor properties ideally suited for large deformations. In addition, most of the preceding work focuses on the nano-/micro-scale strain response of SWNTs (Peng *et al.*, 2001; Minot *et al.*, 2003; Tombler *et al.*, 2000; Dharap *et al.*, 2004; Li *et al.*, 2004). In this study, single-walled carbon nanotube and polyelectrolyte-based (SWNT-PE) multilayer thin films are validated for macro-scale strain sensing. Unlike carbon nanotubes vacuum filtrated and dried to form a thin film of buckypaper, SWNT-PE thin films are multi-phase composite systems consisting of nanotubes and a variety of polyelectroytes. Using a layer-by-layer structure, fabrication parameters can be varied to produce thin films defined by different sensor properties (*e.g.* sensitivity, film resistivity, among others). Unlike buckypaper where linear piezoresistive response is limited to $\varepsilon < 500\ \mu m/m$ (Dharap *et al.*, 2004 and Kang *et al.*, 2006), LbL thin films are high capacity strain sensors (linearity up to $\varepsilon < 10{,}000\ \mu m/m$) (Mamedov *et al.*, 2002 and Loh *et al.*, 2007a). More importantly, the authors experimentally investigate how changes in LbL fabrication parameters can be utilized to tailor and control the aforementioned strain sensor properties. With the aim of fabricating a stand-alone RFID-based strain sensor from multilayer carbon nanotube composites, it is important that the electromechanical properties of the novel material be fully characterized. This study attempts to illuminate the dependencies of SWNT-PE thin film piezoresistivity on both film fabrication parameters and operational signal frequencies.

For characterization, electrical impedance spectroscopy (EIS) is used to deduce an equivalent parallel RC (resistor and capacitor)-circuit model from the electrical response of SWNT-PE thin films tested under applied

mechanical stimuli. The advantage of using impedance spectroscopy is that it identifies frequency-dependent AC (alternating current) circuit parameters typically masked under a time-domain DC (direct current)-based analysis. Upon defining the simple RC-circuit, the same model is utilized to fit SWNT-PE thin film strain sensors in the time-domain under an applied DC current supply. The RC-circuit is further validated by applying different load patterns to multiple samples where the fitted experimental results from both the time- and frequency-domain confirm the validity of the equivalent circuit model. The correlation between changes in strain sensitivity and equivalent circuit model parameters are identified for various fabrication parameters.

SWNT-PE THIN FILM FABRICATION

Layer-by-Layer Assembly

A systematic and controllable layer-by-layer assembly method (Decher *et al.*, 1992; Decher, 1997; Kotov, 2001; Paloniemi *et al.*, 2006) is employed to fabricate multilayer carbon nanotube/polyelectrolyte composite thin films. The LbL method relies on the sequential deposition of alternating charged polycations and polyanions to form homogeneous multilayer thin films upon a glass or silicon substrate as shown in Figure 1a. By controlling the deposition time of the substrate in the charged carbon nanotube and polyelectrolyte solutions, a uniform and controllable-thickness monolayer can be formed. As opposed to creating a stratified multilayer thin film, newly adsorbed polyelectrolytes are capable of interpenetrating previously deposited layers to form multilayer homogeneous composites (Lösche *et al.*, 1998). Adsorption of each monolayer is based on opposite charge electrostatic and van der Waals force attraction to the preceding monolayer (Mamedov *et al.*, 2002; Olek *et al.*, 2004; Rouse and Lillehei, 2003).

In this study, the assembly of SWNT-PE multilayer thin films begins by dipping a clean, charged glass microscope slide (treated with 3:7 H_2O_2:H_2SO_4 piranha solution) into a 1.0 *wt.* % aqueous solution of poly(vinyl alcohol) (PVA, Sigma) to deposit the initial charged polyelectrolyte monolayer. After five minutes, the substrate is removed for rinsing in 18 MΩ deionized water for three minutes and followed by drying for another 10 minutes. Although washing can potentially remove adsorbed polyelectrolytes, Rodriguez *et al*. (2000) has utilized very fast magic-angle spinning nuclear magnetic resonance (MAS NMR) to verify that adsorbed polyelectrolytes remain even after a washing cycle in the LbL process. Next, the deposition of the carbon nanotube monolayer proceeds by dipping the substrate in a SWNT solution for five minutes (ultra-purified HiPCO SWNT from Carbon Nanotechnologies, Inc.). An aqueous solution of poly(sodium 4-styrene-sulfonate) (PSS, 1,000,000 M_w, Aldrich) of various concentrations is employed to provide suspension and dispersion of SWNTs in solution form. Once the substrate has been immersed in the SWNT solution for five minutes, the substrate is rinsed again in 18 MΩ deionized water for three minutes and then dried for another 10 minutes. Yoo *et al.* (1998) have measured each LbL monolayer's thickness (for poly(acrylic acid)/(poly(allylamine) thin films) using a Geartner ellipsometer operating at a wavelength of 633 nm and report that each monolayer's thickness can vary between 1 to 5 nm depending on solution pH. The resulting film exhibits excellent homogeneity and phase integration (*i.e.* no stratification between monolayers is observed) (Decher and Schlenoff, 2003). This process completes one full cycle of the layer-by-layer assembly process to form one bilayer of the SWNT-PE composite thin film (denoted as $(SWNT\text{-}PSS/PVA)_n$, where '*n*' denotes the number of bilayers). The fabrication of multiple bilayers of SWNT-PSS/PVA thin films involves the repetition of the above mentioned process to form multilayer thick films (Figure 1b). Free-standing films of 50, 100, and 200 layers are assembled by the LbL method described (Loh *et al.*, 2007a).

To date, many researchers have employed single-walled and multi-walled carbon nanotubes to enhance the mechanical performance of polymer composite films (Cadek *et al.*, 2004; Frizzell *et al.*, 2005; Wei, 2006; Ajayan *et al.*, 2000). While this study focuses on the piezoresistive characteristics of SWNT-PSS/PVA thin films, mechanical strength strongly influences thin film durability for long-term strain sensing. Although PSS is primarily employed to maximize SWNT dispersion, its high molecular weight simultaneously maximizes mechanical performance (namely, Young's modulus, strength, and fracture toughness) of LbL thin films (Moore *et al.*, 2003). Similar LbL films (fabricated with poly(ethylenimine) and poly(acrylic acid)) have been

mechanically tested and concluded that the ultimate tensile strength is approximately 200 ± 40 MPa (Mamedov *et al.*, 2002).

Suspension and Dispersion of Carbon Nanotubes

Suspension and dispersion of SWNTs in an aqueous solution is necessary for the utilization of the LbL process employed herein. While many researchers have proposed techniques for covalent stabilization of SWNTs, a non-covalent method is selected because this approach does not create defects on nanotube surfaces, thereby preserving the structure, as well as the mechanical and electrical properties of the nanotubes. In general, various surfactants and polymers have been shown to provide non-covalent stabilization and suspension of individual nanotubes while allowing for greater concentration of dispersed carbon nanotubes in solution (Tan and Resasco, 2005). Using mass percent conversion to measure the ability of polymers to disperse SWNTs in solution, Moore *et al.* (2003) validate a wide variety of polymer dispersive agents for carbon nanotubes. In addition, their findings suggest that higher molecular weight polymers with long polymeric chains and hydrophilic groups are inclined to suspend more SWNTs in solution during steric stabilization. Thus, high molecular weight PSS ($M_w \approx 1{,}000{,}000$) is employed to facilitate dispersion of SWNTs in this study. Dispersion is achieved through 180 min of ultrasonication bath (135 W, 42 kHz) followed by 90 min of high-powered tip sonication (3.178 mm tip, 500 W, 22.0 kHz) for 30 min at 30% power output.

PERMUTATION OF FABRICATION PARAMETERS

Earlier studies have demonstrated that SWNT-PE multilayer thin films can be tailored to a wide variety of macro-scale strain sensing properties (Loh *et al.*, 2006). Changes in sensitivity, linearity, and overall film resistivity collectively depend on various layer-by-layer fabrication parameters. Three independent LbL fabrication parameters, namely (1) SWNT concentration (dispersed), (2) PSS concentration, and (3) film thickness (number of bilayers), are varied to correlate their effects toward modifying macro-scale thin film strain sensing properties. In total, 21 unique specimens are constructed from combinations of these three varied fabrication parameters as shown in Table 1.

First, the concentration of single-walled carbon nanotubes in PSS solution is varied. Specifically, three different concentrations will be investigated: 0.25 mg/mL, 0.50 mg/mL, and 0.80 mg/mL (weight per PSS solution volume). Selection of these concentrations is based on experimental studies to provide for adequate dispersion of carbon nanotubes in PSS solutions. Increasing SWNT concentration results in a corresponding increase of SWNT deposition per LbL monolayer. The increase in carbon nanotube deposition creates more nanotube-to-nanotube junctions, thus providing a greater number of paths for electrical current to flow from one electrode to the other while reducing the overall resistivity of the thin film (Stadermann *et al.*, 2004). Furthermore, since SWNTs experience rigid-body motions in the flexible polymer matrix under applied strain (as opposed to deforming axially), more nanotube junctions can participate to enhance strain sensitivity. With increasing nanotube junctions, it is hypothesized that the sensitivity of the thin film to applied strain will increase in tandem while the overall bulk film resistivity will decrease.

While different polymers can facilitate suspension of carbon nanotubes for LbL fabrication, this study will focus on varying concentrations of PSS. It has been determined that the concentration of PSS in solution has a direct effect on the level of carbon nanotube dispersion. To quantify this phenomenon, ten solutions of SWNTs dispersed in increasing concentrations of PSS (0.1%–1.0% by weight) are prepared. Using a UV-Vis spectrophotometer with 10-mm light path cuvettes, absorption spectroscopy is employed to measure the amount of light (wavelength between 300–900 nm) absorbed by the SWNT-PSS solutions (Li *et al.*, 2003). It has been demonstrated that greater nanotube suspension is directly associated with an increase in the UV-Vis resonance peaks as well as the non-resonant background, thus suggesting no preferential dispersion of any particular nanotube (Tan and Resasco, 2005). Figure 2 plots the absorbance at $\lambda = 350$ nm as a function of various concentrations of PSS. The results suggest that a sigmoidal relationship between absorbance and PSS concentration exists and greater nanotube suspension can be achieved by dispersing fixed amounts of SWNTs in higher concentrations of PSS (where 0.7 to 1.0% PSS marks a significant increase in absorbance). To investigate

the effects of dispersion quality on SWNT-PSS/PVA thin film strain sensing properties, three different concentrations of PSS, namely 0.4% (low dispersion), 0.7% (moderate dispersion), and 1.0% PSS (high dispersion) (*wt*. %) have been selected for fabrication. Dispersion of nanotubes is verified with scanning electron microscope (SEM) imagery (Figure 3), showing no deposition of large nanotube bundles and ropes. Furthermore, the SEM image verifies the exceedance of the SWNT percolation threshold (Figure 3).

Another fabrication parameter of interest is the thickness of the SWNT-PSS/PVA thin films themselves. While thicker films can provide additional mechanical strength, it is hypothesized that more layers decrease the overall strain sensitivity of the film due to potentially increased agglomeration during extensive LbL fabrication; clearly, a tradeoff exists between mechanical strength and electrical sensing properties. Thus, three different thicknesses, namely 50, 100, and 200 bilayer thin films, are fabricated to identify changes in SWNT-PSS/PVA thin films' electronic properties. The objective of this optimization study is to identify which fabrication parameters contribute to yield the highest possible strain sensor sensitivity and its associated trends. Furthermore, using time- and frequency-domain analyses, an equivalent circuit model that adequately describes thin film piezoresistive behavior will be most useful for coupling LbL strain sensors with inductively coupled RFID devices.

PIEZORESISTIVITY OF SWNT-PSS/PVA THIN FILMS

Characterization of piezoresistive response of SWNT-PSS/PVA thin films under applied strain is investigated by applying tensile-compressive cyclic load patterns to the SWNT-PSS/PVA samples of Table 1. All 21 thin film specimens are subjected to three different load patterns and load rates, namely (1) a slow, uniform, cyclic tensile-compressive loading at 0.05 mm/sec, (2) a fast load rate of 0.10 mm/sec, and (3) a non-uniform tensile-compressive cyclic load pattern to high strains ($\varepsilon = \pm 10{,}000\ \mu m/m$). Small (2 x 1 cm^2) thin film samples are cut from the glass substrate for electrical-mechanical characterization. These samples are affixed to 3.8 x 30.5 x 1.9 cm^3 PVC (Type I) bars using CN-Y post yield epoxy (Tokyo Sokki Kenkyujo).

To measure the resistance of these thin films, a two-point probe method is established by drying silver paste (Ted Pella) over single-strand wire and the thin film as shown in Figure 4a. Since the typical resistance of SWNT-PSS/PVA thin film samples is on the order of $10^3 - 10^5\ \Omega$, contact resistance can be considered negligible, thereby deeming a four-point probe technique unnecessary. After the silver paste has completely dried (six hours), an MTS-810 load frame is used to apply various tensile-compressive cyclic load patterns to the PVC specimens. The load frame is controlled to apply the three different load patterns to each of the SWNT-PSS/PVA multilayer films (Figure 4b). Resistance change under applied strain is sampled at 1 Hz with an Agilent 34401A digital multimeter supplying 10 μA of DC current. Stroke displacement of the MTS-810 load frame is simultaneously sampled at 1 Hz by the load frame's data acquisition system (DAQ) to provide a baseline comparison of bar strain with experimental data. It should be mentioned that carbon nanotube thin films exhibit sensitivity to light (Loh *et al.*, 2007a) and temperature (Koratkar *et al.*, 2004) (exposure to light and increase in temperature reduce thin film resistance). Thus, to compensate for these external influences to sensor response, thin film testing is conducted in a dark environment while maintaining stable room temperature conditions.

It can be observed from Figures 5 through 8 that SWNT-PSS/PVA thin films exhibit strong piezoresistive behavior irrespective of the applied load pattern. In the first series of tests (Figures 5, 6, and 7), a three-cycle tensile-compressive cyclic load pattern is applied to the specimens to induce ±5,000 μm/m strain. To further investigate the response of SWNT-PSS/PVA thin films to a non-uniform load pattern, the same experiment is conducted with three cycles of ±5,000 μm/m strain applied. Upon reaching ε = 5,000 μm/m on the third cycle, the load frame holds its load for 50 sec before applying two more cycles of tensile-compressive strains ($\varepsilon = \pm 10{,}000$ μm/m) to the specimen. Figure 8 presents a representative experimental time history piezoresistive response of a SWNT-PSS/PVA thin film subjected to the non-uniform load pattern. It can be concluded from all of the tests that SWNT-PSS/PVA thin film resistance is sensitive to strain.

However, one intrinsic issue with measuring thin film resistance has been identified and that is a time-dependent exponential decay in resistance regardless of applied loading (self-evident in Figures 5 through 8). Although film resistance decay may not seem exponential (in Figures 5 through 8), the exponential decay occurs over long periods of time (six to seven hours) before reaching its steady-state resistance (Figure 9); strained time

history records shown in Figures 5 through 8 occur over minutes, thus masking the overall exponential film resistance decay. Furthermore, despite applying a saw-tooth tensile-compressive cyclic load pattern, the corresponding strain sensor response shows considerable distortion of the input waveform as observed from the rounded peaks (approaching that of a sinusoidal signal). Identification of the source of distortion will be conducted with a frequency-domain-based analysis (*i.e.* electrical impedance spectroscopy); it will become apparent in later discussions that the distortion is due to a parallel RC-circuit (resistor and capacitor)-type behavior.

Time Dependent Exponential Resistivity Decay

Experimental studies using both a two-point and a four-point measurement probe technique indicate that SWNT-PSS/PVA thin films show an exponential decay in bulk resistance as a function of time. While the nature of this decay is unknown, it is hypothesized that various factors contribute to the slow resistivity decay. For example, the applied DC current source (*i.e.* the Agilent 34401A digital multimeter supplies a constant current of $i = 10$ μA) causes a rise in film temperature over time. In a previous study (Loh *et al.*, 2007a), it has been verified that different magnitudes of applied current changes the time-dependent exponential decay rate of SWNT-PSS/PVA film resistance. Vincent *et al.* (2002) report individual chemical vapor deposition (CVD)-grown nanotubes exhibit Joule heating across its length. When subjected to current in the microampere range (*e.g.* 2 μA), the temperature for a 40 μm long nanotube can reach 1,900 K. In addition, the temperature along the carbon nanotube length is directly proportional to the different magnitudes of applied current. It is speculated that localized heating between nanotube-to-nanotube junctions slowly activates electrons to tunnel between unconnected tubes, thus increasing film conductivity (thereby decreasing resistivity). Furthermore, thermal-assisted chemical recombination at nanotube junctions can chemically modify carbon nanotube junctions to form permanent bridges and ultimately lowering bulk film resistance. In addition to the aforementioned physical processes, current-induced chemical changes may also occur within the carbon nanotube-polymer composite to contribute to the observed changes in resistance over time. Nevertheless, the exponential resistance decay can be modeled accurately using a standard exponential decay model of the form $R = Ge^{Ht}+C$ as shown in Figure 9.

FREQUENCY DOMAIN DERIVATION OF AN EQUIVALENT CIRCUIT MODEL

Although an equivalent circuit model can be derived to fit the time history resistance of the film under strain (as shown in Figures 5 through 8), such a crude time-domain approach might neglect to identify frequency-dependent equivalent circuit elements. Another reason for ensuring the equivalent circuit model reflects the frequency-dependent properties of the thin films is that some sensing applications might require the film to be electrically queried using AC signals. For example, SWNT-PSS/PVA thin films can be patterned as inductive coil antennas (Figure 10) for use as a conformable RFID-style sensor. For example, our current work is already exploring the inductive coupling effect between SWNT-PSS/PVA thin film coil antennas patterned on a substrate and a remote RFID reader; the resonant frequency and bandwidth of the inductive coupling effect would change with strain (Loh *et al.*, 2007b).

Using techniques such as electrical impedance spectroscopy (EIS), one can characterize the frequency dependent electrical properties of materials and their interfaces (Barsoukov and Macdonald, 2005). The motivation for using EIS in this study is to identify the frequency-dependent electrical behavior of SWNT-PSS/PVA thin films which may be masked under the DC time-domain approach previously used. Combined with physical observations from the DC time-domain approach (*i.e.* identification of the time-dependent exponentially decaying film resistance), a simple and unique equivalent circuit (and its associated resistance, capacitance, and inductance) can be deduced from the frequency-domain response of a material under study. Subsequently, the derived circuit model from EIS can be used to validate the DC electrical response of loaded thin films previously obtained.

Electrical Impedance Spectroscopy

In EIS, impedance measurements are taken by applying a monochromatic AC electrical stimulus of known voltage ($v(t) = V_{in}sin(\omega t)$) and frequency ($f = \omega/2\pi$) and measuring the corresponding steady-state current response of the system ($i(t) = I_{out}sin(\omega t+\theta)$ where θ is the phase difference between voltage and current). While a time-domain analysis can extract material behavior due to an AC stimulus, the relationship between input stimulus and output response is very complex and requires differential equations to explain. On the other hand, impedance measurements (by definition a complex quantity denoted as $Z(\omega) = Z' + jZ''$), inherently take the phase difference and attenuation between input and output into account. In rectangular coordinates, the real and imaginary components of impedance, $Z(\omega)$, can be expressed as:

$$\mathrm{Re}(Z) \equiv Z' = |Z|\cos(\theta) \tag{1a}$$

$$\mathrm{Im}(Z) \equiv Z'' = |Z|\sin(\theta) \tag{1b}$$

Typically, an automated frequency response analyzer (FRA) can be employed to perform impedance spectroscopy. Its operating principle is simple; a sine-wave perturbation ($P(t) = P_0 sin(\omega t)$) is applied to the material, and its corresponding cell response is correlated to two synchronous signals, where one signal is in-phase while the other is 90º out-of-phase with the input signal. For a given frequency, ω, the complex impedance can be extracted by integrating the cell transfer function and cell response over a certain number of periods (N_f) of the input sinusoidal perturbation (Barsoukov and Macdonald, 2005). An attractive feature of most FRAs is their ability to sweep through a set of frequencies when measuring impedance.

Equivalent Circuit Modeling

In this study, the Solartron 1260 impedance gain/phase analyzer is selected to serve as an FRA for electrical characterization of SWNT-PSS/PVA thin films. To measure the complex impedance of the films, the Solartron 1260 uses a four-probe technique and outputs an AC sine-wave perturbation with amplitude of 3.0 V. The input stimuli frequency (ω) is varied between 15 – 250 kHz to capture the specimen's frequency-domain response. Upon subjecting the 21 fabricated films (Table 1) to EIS, all SWNT-PSS/PVA multilayer films yield a typical semicircular response in the complex impedance plane (commonly termed the Cole-Cole plot) which is consistent with a parallel RC-circuit (as opposed to being purely resistive or capacitive); an example Cole-Cole plot of a $(SWNT\text{-}PSS/PVA)_{50}$ thin film is shown in Figure 11.

In order to determine a unique equivalent circuit model that describes SWNT-PSS/PVA multilayer films in both the frequency and time domain, a stochastic simulated annealing model-updating algorithm (Duda *et al.*, 2001) is employed to numerically fit different parallel RC-circuit models to the experimental Cole-Cole plots. The objective function embedded in the simulated annealing model-updating method seeks to minimize the sum of the least-squares difference between numerical (derived from an equivalent circuit model) and experimental (from EIS) complex impedance data. From simulated annealing fitting of multiple variations of parallel RC-circuit models, one equivalent circuit model is selected to describe the behavior of SWNT-PSS/PVA thin films. The proposed equivalent circuit model is shown in Figure 12, and a representative model-updated Cole-Cole plot fit is overlaid with the experimental plot in Figure 11. The equivalent circuit model identifies three discrete circuit elements: a series resistor (R_o), a parallel resistor (R_i), and a parallel capacitor (C_i).

Previously, it has been shown that the bulk SWNT-PSS/PVA thin film resistance changes upon applied strain (Figures 5 – 8) while exhibiting a time-dependent exponential decay in film resistance (Figure 9). Accurate incorporation of these DC time-domain observations into the EIS-derived equivalent circuit model is accomplished by observing how changes in equivalent circuit element parameters change the overall complex impedance response in the frequency domain. Figure 12 shows a schematic as to how these changes (namely R_o, R_i, and C_i) lead to changes in SWNT-PSS/PVA frequency response.

First, in order to identify the equivalent resistor sensitive to the exponential decay effect, multiple EIS analyses are performed one after another on unloaded SWNT-PSS/PVA specimens; each sequential EIS analysis is performed a constant time (t_i) after the previous analysis. The resulting frequency response shows that as time increases, each corresponding Cole-Cole plot shifts towards decreasing real impedance (Figure 13), thus

identifying R_0 and R_i as responsible for modeling the DC exponential decay in film resistance (Figure 9). Furthermore, the equivalent capacitor C_i also exhibits exponential decay during impedance spectroscopy analysis and can be modeled as $C_i = C_t - Ae^{Bt}$. While the nature of change in capacitance is undetermined, it is hypothesized that the applied current source (from DC resistance measurements and AC EIS analysis) increases the probability of electron tunneling between neighboring carbon nanotubes, thus reducing film capacitance and resistance. Whereas the exponential decay in resistance (R_i) can be identified in the DC time-domain approach, changes in capacitance cannot be easily identified. The discovery of the exponentially decaying C_i illustrates the superiority of combining time- and frequency-domain analyses for the derivation of an accurate equivalent circuit model.

Secondly, identification of the strain-sensitive equivalent circuit element is conducted by applying a one-cycle tensile-compressive load pattern ($\varepsilon = \pm 5{,}000\ \mu m/m$) to the thin films similar to that previously mentioned in this paper. The load frame displacement is held at every $\varepsilon = 2{,}500\ \mu m/m$ intervals (0.25% strain) to capture the EIS response of the SWNT-PSS/PVA thin films. A total of nine EIS analyses are taken during this one load cycle as shown in Figure 14. The corresponding Cole-Cole plots at each strain-state are overlaid and shown in Figure 15, where the leftward shift is due to the exponential decay of film resistance (R_0 and R_i) caused by an applied current stimulus.

Extraction of the strain-sensitive equivalent circuit parameter is accomplished by observing any strain sensitivity in each of the individual circuit elements (R_o, R_i, and C_i). Meticulous scrutiny of strained experimental data confirms that the parallel resistor R_i is sensitive to strain. By calculating the time between each EIS test, one can plot the progressive decrease of Z_{real} as a function of time (Figure 16a) with each data point corresponding to a particular strain-state experienced by the SWNT-PSS/PVA thin films. Upon removal of the exponential decay in Z_{real} by post-processing the experimental data, it can be shown in Figure 16b that SWNT-PSS/PVA thin films' Z_{real} exhibit near-linear sensitivity to changes in strain. To model the piezoresistivity of R_i in the proposed equivalent circuit model (Figure 12), resistive strain sensitivity (S_R) can be defined and calculated

$$S_R = \frac{\Delta R(\varepsilon)/R_t}{\varepsilon} \tag{2}$$

where ε is uniaxial strain in the SWNT-PSS/PVA thin film.

In total, ten unique variables are required to model the behavior of SWNT-PSS/PVA thin films in the time- and frequency-domain. These equivalent circuit parameters are identified as: (1) the discrete circuit element values R_s, C_t, and R_t; (2) the exponential decay coefficients A and B for C_i, K and L for R_i, and G and H for R_o (Figure 12); and (3) S_R defined as the strain sensitivity of the SWNT-PSS/PVA thin film. Using these ten parameters and the equivalent circuit model shown in Figure 12, the equivalent complex impedance ($Z_{eq}(\omega)$) can be calculated easily as shown in equation 3.

$$Z_{eq}(\omega) = R_s + Ge^{Ht} + \frac{1}{\left[\left(R_t + Ke^{Lt}\right)\left(1 + S_R\varepsilon\right)\right]^{-1} + i\omega\left(C_t - Ae^{Bt}\right)} \tag{3}$$

Equation 3 is employed to calculate the equivalent circuit complex impedance for simulated annealing fitting of experimental SWNT-PSS/PVA thin film frequency response.

RESULTS AND DISCUSSION

Frequency-Domain EIS Analysis on Unloaded SWNT-PSS/PVA Thin Films

Using a Solartron 1260 impedance gain/phase analyzer coupled with the same experimental setup mentioned earlier, EIS analysis is conducted for all 21 films fabricated (Table 1). The purpose for conducting frequency-domain analyses on unloaded SWNT-PSS/PVA multilayer films is to identify the correlation between LbL fabrication parameters and equivalent circuit parameters. All EIS experimental data is fitted to the equivalent

circuit model (Figure 12) through the simulated annealing algorithm. By calculating the equivalent complex impedance (Equation 3) and minimizing the sum of the least-squares difference between numerical and experimental data, simulated annealing converges to output values for the ten unique equivalent circuit parameters (R_s, R_t, C_t, A, B, G, H, K, L, and S_R). Equivalent circuit parameters exhibit consistent trends with changes in the LbL fabrication parameters. For example, consider R_s and R_t; results from the frequency-domain model fitting are tabulated in Table 2 and graphically shown in Figure 17. Valid side-by-side comparison between fitted circuit parameters for different films are made possible by normalizing film resistance with its surface area (R_{fitted} = [Ω/cm^2]). This normalization is necessary since films might be cut to slightly different sizes.

In general, results show that the model-fitted values for R_s and R_t follow well-defined trends. First, as carbon nanotube concentration is increased from 0.25 mg/mL to 0.80 mg/mL, a progressive decrease in R_s and R_t is observed due to increased nanotube-to-nanotube junctions corresponding to greater carbon nanotube concentration (in solution) (Figure 17a). Also, increasing PSS concentrations causes increasing equivalent resistances potentially due to greater polyelectrolyte adsorption during LbL (Figure 17b). Finally, with increasing film thicknesses, resistance decreases; this phenomenon can be explained by assuming each bilayer as a parallel resistor, where every additional resistor to the parallel network causes an overall decrease in resistance. Using this data derived from EIS analysis on unloaded SWNT-PSS/PVA thin films, one can begin to tailor films with specific impedance and frequency-dependent properties by simply varying LbL fabrication parameters.

Time-Domain Strained SWNT-PSS/PVA Thin Film Response

Using the MTS-810 input tensile-compressive cyclic load pattern, theoretical calculations from the equivalent circuit model is fitted with the experimental, strained SWNT-PSS/PVA resistance time histories. The simulated annealing model updating algorithm is carried through for all 21 SWNT-PSS/PVA films fabricated and tested (Table 1) in order to numerically fit the proposed equivalent circuit model (Figure 12) to the experimental time history results as shown in Figure 18. It can be observed that the equivalent circuit model fitted with the simulated annealing algorithm describes the thin film response well, and the proposed equivalent RC-parallel circuit model is adequate in modeling SWNT-PSS/PVA changes in resistance to applied strain in both the frequency- and time-domains (Figures 11 and 18, respectively). Furthermore, it has been identified that the distortion of the input saw-tooth waveform as observed in the rounded peaks in the collected resistance time histories is due to the parallel capacitance.

Variation in Strain Sensitivity to Fabrication Parameters

Of greatest interest is the dependency of LbL fabrication parameters to changes in SWNT-PSS/PVA strain sensitivity (S_R, given in equation 2). As one of the ten unknown variables during simulated annealing model fitting, S_R can be extracted and compared for all 21 films fabricated with a different combination of LbL fabrication parameters (Table 1). Among the various thin films load-tested, strong trends can be identified between strain sensitivity (S_R) and the LbL fabrication parameters (namely SWNT concentration, PSS concentration, and the thin film thickness) (Table 3a-c).

First, as SWNT concentration is increased from 0.25 to 0.80 mg/mL, the strain sensitivity of the thin film increases irrespective of the number of layers and PSS concentration; this can be observed by considering each row of Tables 3a-c and Figure 19. Stadermann *et al.* (2004) show that as carbon nanotube content is increased, local conductance of the thin film relies heavily on the number of nanotube-to-nanotube junctions. The increased nanotube junctions present in higher SWNT concentration thin films allow for higher strain sensitivity as the films are stretched or compressed axially. Not only does thin film nominal resistance decrease due to greater nanotube deposition during LbL assembly to give rise to higher sensitivity (*i.e.* larger relative change in resistance to nominal film resistance), but also, it is hypothesized that deformations due to strain will cause rigid-body motion of nanotubes in this flexible polymer composite matrix (as opposed to SWNTs deforming axially due to strain). For instance, upon applying tensile strain, individual SWNTs displace in the polymer matrix, thereby reducing the number of nanotube-to-nanotube junctions to cause an increase in resistance to give rise to the piezoresistive nature of these SWNT-PSS/PVA thin films (the contrary is applicable for compressive strains).

Therefore, with increasing nanotube deposition, more nanotube-to-nanotube junctions can participate during applied strain to cause changes in film resistance to increase strain sensitivity. This trend exists for films fabricated with different thicknesses and PSS concentrations and is consistent between the two different load rates of 0.10 and 0.05 mm/sec (Figure 19).

Furthermore, SWNT-PSS/PVA thin films exhibit increasing strain sensitivity as the PSS dispersing agent concentration (*by wt.*) is increased. From the UV-Vis plot of absorbance as a function of PSS concentration (Figure 2), it has been shown that suspension of carbon nanotubes is facilitated with higher PSS concentrations. Due to the weak electrostatic and van der Waals force attraction between each additional monolayer, large nanotube bundles cannot be deposited during the LbL fabrication process. Thus, greater dispersion of nanotubes in higher PSS concentration solutions allow for more individually suspended or small bundles of nanotubes to adsorb onto the thin film while creating more nanotube-to-nanotube junctions to achieve higher strain sensitivity. From each column of Table 3 and Figure 20, an interesting phenomenon can be observed; 50-bilayer thin films' strain sensitivities are plateauing as the dispersing agent's (PSS) concentration is increased from 0.4% to 1.0%. On the contrary, 100- and 200-bilayer thin films exhibit remarkable increases in strain sensitivity as PSS concentration is increased. While strain sensitivity for these films may eventually plateau, further increasing PSS concentration can potentially achieve even higher sensitivities. It should be noted that a more detailed analysis with additional specimens needs to be conducted to provide greater resolution of trends in Figure 20.

Finally, as film thickness is increased, the strain sensitivity for films of the same PSS and SWNT concentration progressively decreases. Yet, experiments conducted with free-standing LbL films suggest an increase in mechanical strength and ultimate strain capacity with increasing film thickness. A tradeoff exists between optimizing SWNT-PSS/PVA thin films for higher sensitivity at the cost of lower ultimate strain capacity or vice versa. Although this study has been conducted with only 21 unique thin film specimens, thus providing for a limited number of data points in Figures 19 and 20, this study focuses on identifying trends in commonly-used ranges in each fabrication parameter (*i.e.* SWNT and PE concentration and film thickness) (Table 1). In the near future, additional thin film samples will be conducted to provide a more detailed analysis for optimization.

Drift-Free Dynamic Strain Measurements

The inherent time-dependent resistance decay appears to be a limitation of the SWNT-PSS/PVA strain sensor. However, the rate of decay is sufficiently slow, such that a high-pass circuit can be used to remove the slow resistance decay. For this purpose, a 4-pole Bessel band-pass filter is proposed for the SWNT-PSS/PVA thin films. A signal conditioning circuit board with a 4-pole Bessel filter (with a pass-band between 0.014 and 25 Hz) is adopted (Figure 21a) (Horowitz and Hill, 2001). Validation of this experimental setup is conducted by applying another 20-cycle tensile-compressive cyclic load pattern to strain SWNT-PSS/PVA thin films using the band-pass circuit. A representative portion of the time history is presented in Figure 21b; the band-pass circuit is effective in removing the resistance decay without distorting the strain measurement signal.

Through the use of a 4-pole Bessel filter, which typically requires complex circuitry, the resulting SWNT-PSS/PVA thin film strain sensor loses its characteristics as a miniature thin film sensor. Since the ultimate goal of this research is to develop a complete layer-by-layer-assembled RFID wireless sensor, a different approach is required to attain drift-free sensor response. Instead of using a charged glass substrate during LbL self-assembly, a poly(ethylene terephthalate) (PET, 3M) thin film (0.127 mm thick) can be employed as the LbL substrate. Following the same experimental thin film fabrication procedure, a carbon-nanotube based parallel capacitor is formed (where PET acts as the dielectric that separates the two conducting SWNT-PSS/PVA thin films on each side of the substrate). The capacitance of this SWNT-parallel capacitor (denoted as SWNT-on-PET) can be calculated via equation 4.

$$C_{SWNT-on-PET} = \frac{\varepsilon_r \varepsilon_0 wL}{g}\left(1+\varepsilon_s\right) \tag{4}$$

where ε_r is the relative dielectric permittivity of PET, ε_0 is the permittivity of air ($\varepsilon_0 = 8.854 \cdot 10^{-12}$ *F/m*), w (width) and L (length) are the dimensions of the SWNT-on-PET capacitor, g is 0.127 mm (PET thickness), and ε_s is the applied strain. From equation 4, it is obvious that SWNT-on-PET capacitance is linearly related to strain, while capacitance can be adjusted by controlling sample dimensions (Figure 22a). Upon affixing a SWNT-on-PET capacitive strain sensor to a PVC (Type I) bar and subsequently measuring sensor response with the Solartron 1260 impedance gain/phase analyzer to an applied tensile-compressive cyclic load pattern (Figure 14, from -10,000 to 7,500 μm/m strains), it can be seen from Figure 22b that capacitance change is linearly related to applied strain. Thus, SWNT-on-PET thin films can be utilized as capacitive strain sensors in order to obtain drift-free strain measurements without complex circuitry.

CONCLUSIONS

Results from this study allow one to begin tailoring the design of an SWNT-PSS/PVA thin film strain sensor using a "bottom-up" approach. In this study, a layer-by-layer method is employed to fabricate a diverse suite of SWNT-PSS/PVA thin films composed of varying combinations of SWNT concentration, PSS concentration, and film thickness. The purpose of this study is to experimentally characterize changes in LbL fabrication parameters and correlate them to bulk material strain sensing properties. Based on identified trends between fabrication parameters and thin film piezoresistivity, one can begin to fabricate nanotube-based strain sensors using a "bottom-up" technique where desired sensing properties are attained by simple manipulation of the processing of SWNTs at the molecular-scale.

An RC-circuit model is devised from frequency-domain electrical impedance spectroscopy to fit experimental data to numerical results in both the frequency- and time-domains. Circuit parameters such as the strain-sensitive resistance, film capacitance, and exponentially decaying parameters that simulate the exponential decay of film resistance are all fitted using a simulated annealing algorithm to minimize the sum of least-squares difference between experimental and analytical resistance time-histories. SWNT-PSS/PVA thin films fabricated on glass substrates are cut into small rectangles and mounted to PVC bars subjected to tensile-compressive cyclic loading to ±1.0% strains ($\varepsilon = \pm 10{,}000\ \mu m/m$). Results of the fit from both the frequency- and time-domains suggest the equivalent RC-circuit model describes the strained SWNT-PSS/PVA thin film well. Despite the presence of a time-dependent exponential decay of film resistance, two methods can be employed to obtain a drift-free sensor response. First, a band-pass (between 0.014 – 25 Hz) signal-conditioning circuit is included to experimentally filter out this inherent nonlinear property of SWNT-PSS/PVA thin films. On the other hand, SWNT-PSS/PVA thin films can be deposited on PET substrates to form a capacitive strain sensor such that when coupled with an RFID system, strain sensor response is correlated with capacitance. Most importantly, unique trends are observed, where increasing carbon nanotube and/or PSS concentration during LbL fabrication increases the overall film strain sensitivity. The increase in nanotube concentration and subsequent LbL deposition creates more nanotube-to-nanotube junctions, allowing the SWNT-PSS/PVA film to be more sensitive to strain. Enhanced dispersion for higher PSS concentrations allows for larger quantities of individual nanotubes to be deposited on the substrate, thus increasing the SWNT-PSS/PVA thin film strain sensitivity.

ACKNOWLEDGEMENTS

This research is funded by the National Science Foundation (Grant Number CMS – 0528867). The authors would like to express their gratitude to Professor Victor Li and the ACE-MRL group at the University of Michigan for allowing us to use their MTS-810 load frame during the experimental phase of this study. The authors would also like to thank Mr. Andrew Zimmerman for assistance with simulated annealing model updating.

REFERENCES

Ajayan, P. M., Schadler, L. S., Giannaris, C., and Rubio, A. 2000. "Single-walled carbon nanotube-polymer composites: strengths and weaknesses," *Advanced Materials*, **12**: 750-753.

Andrews, R., Jacques, D., Rao, A. M., Rantell, T., Derbyshire, F., Chen, Y., Chen, J., and Haddon, R. C. 1999. "Nanotube composite carbon fibers," *Applied Physics Letters*, **75**: 1329-1331.

Barsoukov, E. and Macdonald, J. R. ed. 2005. *Impedance spectroscopy theory, experiment, and applications*, 2nd Edn, John Wiley & Sons: Hoboken, NJ.

Baughman, R. H., Zakhidov, A. A., and de Heer, W. A. 2002. "Carbon nanotubes – the route towards applications," *Science*, **297**: 787-792.

Cadek, M., Coleman, J. N., Ryan, K. P., Nicolosi, V., Bister, G., Fonseca, A., Nagy, J. B., Szostak, K., Beguin, F., and Blau, W. J. 2004. "Reinforcement of polymers with carbon nanotubes: the role of nanotube surface area," *Nano Letters*, **4**: 353-356.

Chen, R. J., Franklin, N. R., Kong, J., Cao, J., Tombler, T. W., Zhang, Y., and Dai, H. 2001. "Molecular photodesorption from single-walled carbon nanotubes," *Applied Physics Letters*, **79**: 2258-2260.

Dai, L. 2002. "Carbon nanotube sensors," *Proceedings of SPIE – 9th Annual International on Smart Structures and Materials*, **4695**: 237-244.

Decher, G. 1997. "Fuzzy nanoassemblies toward layered polymeric multicomposites," *Science*, **277**: 1232-1237.

Decher, G. and Schlenoff, J. B. 2003. *Multilayer Thin Films: Sequential Assembly of Nanocomposite Materials*, Wiley-VCH: Federal Republic of Germany.

Decher, G., Hong, J-D., and Schmitt, J. 1992. "Buildup of ultrathin multilayer films by a self-assembly process: III. consecutively alternating adsorption of anionic and cationic polyelectrolytes on charges surfaces," *Thin Solid Films*, **210/211**: 831-835.

Dharap, P., Li, Z., Nagarajaiah, S., and Barrera, E. V. 2004. "Nanotube film based on single-wall carbon nanotubes for strain sensing," *Nanotechnology*, **15**: 379-382.

Duda, R. O., Hart, P. E., and Stork, D. G. 2001. *Pattern Classification*, Wiley: New York, NY.

Frizzell, C. J., in het Panhuis, M., Coutinho, D. H., Balkus Jr., K. J., Minett, A. I., Blau, W. J., and Coleman, J. N. 2005. "Reinforcement of macroscopic carbon nanotube structures by polymer intercalation: the role of polymer molecular weight and chain conformation," *Physical Review B*, **72**: 245420/1-245420/8.

Horowitz, P. and Hill, W. 1989. *The Art of Electronics*, 2nd Edn., Cambridge University Press:

Iijima, S. 1991. "Helical microtubules of graphitic carbon," *Nature*, **354**: 56-58.

Jia, Y. and Sun, K. 2006. "Thick film wireless and powerless strain sensor," *Proceedings of SPIE – Smart Structures and Materials*, **6174**: 61740Z/1-61740Z/11.

Kang, I., Schulz, M. J., Kim, J. H., Shanov, V., and Shi, D. 2006. "A carbon nanotube strain sensor for structural health monitoring," *Smart Materials and Structures*, **15**: 737-748.

Kong, J., Franklin, N. R., Zhou, C., Chapline, M. G., Peng, S., Cho, K., and Dai, H. 2000. "Nanotube molecular wires as chemical sensors," *Science*, **287**: 622-625.

Koratkar, N., Modi, A., Lass, E., and Ajayan, P. 2004. "Temperature effects on resistance of aligned multiwalled carbon nanotube films," *Journal of Nanoscience and Nanotechnology*, **4**(7): 744-748.

Kotov, N. A. 2001. "Ordered layered assemblies of nanoparticles," *MRS Bulletin*, **26**: 992-997.

Lanzara, G. and Chang, F-K. 2005. "Nano-deformation sensing with carbon nanotube film," *Proceedings of the 5th International Workshop on Structural Health Monitoring*, 860-870.

Li, X-H., Wu, B., Huang, J-E., Zhang, J., Liu, Z-F., and Li, H-L. 2003. "Fabrication and characterization of well-dispersed single-walled carbon nanotube/polyaniline composites," *Carbon*, **41**(8): 1670-1673.

Li, Z., Dharap, P., Nagarajaiah, S., Barrera, E. V., and Kim, J. D. 2004. "Carbon nanotube film sensors," *Advanced Materials*, **16**: 640-643.

Loh, K. J., Kim, J., Lynch, J. P., Kam, N. W. S., and Kotov, N. A. 2007a. "Multifunctional layer-by-layer carbon nanotube-polyelectrolyte thin films for strain and corrosion sensing," *Smart Materials and Structures*, **16**, 429-438.

Loh, K. J., Lynch, J. P., and Kotov, N. A. 2006. "Mechanical-electrical characterization of carbon nanotube thin films for structural monitoring applications," *Proceedings of SPIE – Smart Structures and Materials*, **6174**: 61741Z-617412Z.

Loh, K., Lynch, J. P., and Kotov, N. A. 2007b. "Passive wireless strain and pH sensing using carbon nanotube-gold nanocomposite thin films," *Proceedings of SPIE – Smart Structures and Materials*, **6529** (*submitted*).

Lösche, M., Schmitt, J., Decher, G., Bouwman, W. G., and Kjaer, K. 1998. "Detailed structure of molecularly thin polyelectrolyte multilayer films on solid substrates as revealed by neutron reflectrometry," *Macromolecules*, **31**: 8893-8906.

Maiti, A., Svizhenko, A., and Anantram, M. P. 2002. "Electronic transport through carbon nanotubes: effects of structural deformation and tube chirality," *Physical Review Letters*, **88**: 126805/1-126805/4.

Mamedov, A. A., Kotov, N. A., Prato, M., Guldi, D. M., Wicksted, J. P., and Hirsch, A. 2002. "Molecular design of strong single-wall carbon nanotube/polyelectrolyte multilayer composites," *Nature Materials*, **1**: 190-194.

Meyyappan, M. ed. 2005. *Carbon nanotubes science and applications*, CRC Press: Boca Raton, FL.

Minot, E. D., Yaish, Y., Szaonova, V., Park, J-Y., Brink, M., and McEuen, P. L. 2003. "Tuning carbon nanotube bad gaps with strain," *Physical Review Letters*, **90**: 156401/1-156401/4.

Mita, A. and Takahira, S. 2002. "Health monitoring of smart structures using damage index sensors," *Proceedings of SPIE – Smart Structures and Materials*, **4696**: 92-99.

Mita, A. and Takahira, S. 2003. "A smart sensor using a mechanical memory for structural health monitoring of a damage-controlled building," *Smart Materials and Structures*, **12**(2): 204-209.

Mita, A. and Takahira, S. 2004. "damage index sensors for smart structures," *Structural Engineering and Mechanics*, **17**(3-4): 331-346.

Moore, V. C., Strano, M. S., Haroz, E. H., Hauge, R. H., and Smalley, R. E. 2003. "Individually suspended single-walled carbon nanotubes in various surfactants," *Nano Letters*, **3**: 1379-1382.

Olek, M., Ostrander, J., Jurga, S., Mohwald, H., Kotov, N., Kempa, K., and Giersig, M. 2004. "Layer-by-layer assembled composites from multiwall carbon nanotubes with different morphologies," *Nano Letters*, **4**: 1889-1895.

Paloniemi, H., Lukkarinen, M., Aaritalo, T., Areva, S., Leiro, J., Heinonen, M., Haapakka, K., and Luddari, J. 2006. "Layer-by-layer electrostatic self-assembly of single-wall carbon nanotube polyelectrolytes," *Langmuir*, **22**: 74-83.

Peng, S., O'Keeffe, J., Wei, C., Cho, K., Kong, J., Chen, R., Franklin, N., and Dai, H. 2001. "Carbon nanotube chemical and mechanical sensors," *Proceedings of the 3rd International Workshop on Structural Health Monitoring*, 1-8.

Rodriguez, L. N. J., De Paul, S. M., Barrett, C. J., Raven, L., and Spiess, H. W. 2000. "Fast magic-angle spinning and double-quantum H solid state NMR spectroscopy of polyelectrolyte multilayers," *Advanced Materials*, **12**(24): 1934-1938.

Rouse, J. H. and Lillehei, P. T. 2003. "Electrostatic assembly of polymer/single walled carbon nanotube multilayer films," *Nano Letters*, **3**: 59-62.

Salvetat, J-P., Bonard, J-M., Thomson, N. H., Kulik, A. J., Forro, L., Benoit, W., and Zuppiroli, L. 1999. "Mechanical properties of carbon nanotubes," *Appl. Phys. A*, **69**: 255-260.

Stadermann, M., Papadakis, S. J., Falvo, M. R., Novak, J., Snow, E., Fu, Q., Liu, J., Fridman, Y., Boland, J. J., Superfine, R., and Washburn, S. 2004. "Nanoscale study of conduction through carbon nanotube networks," *Physical Review B*, **69**: 201402/1-201402/3.

Stein, P. K. 2006. "1936 – A banner year for strain gages and experimental stress analysis – an historical perspective," *Experimental Techniques*, **30**: 23-41.

Tan, Y. and Resasco, D. E. 2005. "Dispersion of single-walled carbon nanotubes of narrow diameter distribution," *J. Phys. Chem. B.*, **109**: 14454-14460.

Todd, M. 2005. "Different approaches towards deploying SHM sensor arrays: wireless communications with autonomous vehicle interrogation," *Proceedings of the 5th International Workshop on Structural Health Monitoring*, 1594-1601.

Tombler, T. W., Zhou, C., Alexseyev, L., Kong, J., Dai, H., Liu, L., Jayanthi, C. S., Tang, M., and Wu, S-Y. 2000. "Reversible electromechanical characteristics of carbon nanotubes under local-probe manipulation," *Nature*, **405**: 769-772.

Tsukagoshi, K., Yoneya, N., Uryu, S., Aoyagi, Y., Kanda, A., Ootuka, Y., and Alphenaar, B. W. 2002. "Carbon nanotube devices for nanoelectronics," *Physica B*, **323**: 107-114.

Vincent, P., Purcell, S. T., Journet, C., and Binh, V. T. 2002. "Modelization of resistive heating of carbon nanotubes during field emission," *Physical Review B*, **66**: 075406/1-075406/5.

Wei, C. 2006. "Adhesion and reinforcement in carbon nanotube polymer composite," *Applied Physics Letters*, **88**: 093108/1-3.

Wood, J. R., Zhao, Q., Frogley, M. D., Meurs, E. R., Prins, A. D., Peijs, T., Dunstan, D. J., and Wagner, H. D. 2000. "Carbon nanotubes: from molecular to macroscopic sensors," *Physical Review B*, **62**(11): 7571-7575.

Yoo, D., Shiratori, S. S., and Rubner, M. F. 1998. "Controlling bilayer composition and surface wettability of sequentially adsorbed monolayers of weak polyelectrolytes," *Macromolecules*, **31**: 4309-4318.

Table 1. Matrix of 21 unique SWNT-PSS/PVA thin films fabricated

	0.25 mg/mL SWNT	**0.50 mg/mL SWNT**	**0.80 mg/mL SWNT**
$(SWNT\text{-}PSS/PVA)_{50}$	0.4, 0.7, and 1.0% PSS	0.4, 0.7, and 1.0% PSS	0.4, 0.7, and 1.0% PSS
$(SWNT\text{-}PSS/PVA)_{100}$	0.4, 0.7, and 1.0% PSS	0.4, 0.7, and 1.0% PSS	0.4, 0.7, and 1.0% PSS
$(SWNT\text{-}PSS/PVA)_{200}$	-	0.4, 0.7, and 1.0% PSS	-

Table 2. (a) Model-updated equivalent circuit model fitted R_s values (Ω/cm^2).

0.4% PSS	**0.25 mg/mL SWNT**	**0.50 mg/mL SWNT**	**0.80 mg/mL SWNT**
50 bilayers	12,107.0	10,557.6	8,920.7
100 bilayers	5,921.8	891.9	854.0
0.7% PSS	**0.25 mg/mL SWNT**	**0.50 mg/mL SWNT**	**0.80 mg/mL SWNT**
50 bilayers	62,472.2	15,183.6	15,063.5
100 bilayers	14,083.8	4,589.7	3,370.2
1.0% PSS	**0.25 mg/mL SWNT**	**0.50 mg/mL SWNT**	**0.80 mg/mL SWNT**
50 bilayers	66,489.0	65,470.7	27,595.8
100 bilayers	28,412.9	11,241.2	6,889.9

Table 2. (b) Model-updated equivalent circuit model fitted R_t values (Ω/cm^2).

0.4% PSS	**0.25 mg/mL SWNT**	**0.50 mg/mL SWNT**	**0.80 mg/mL SWNT**
50 bilayers	5,303.9	5,084.4	4,850.6
100 bilayers	2,661.7	422.6	380.9
0.7% PSS	**0.25 mg/mL SWNT**	**0.50 mg/mL SWNT**	**0.80 mg/mL SWNT**
50 bilayers	28,043.4	7,334.8	6,929.9
100 bilayers	7,580.5	2,022.6	1,519.1
1.0% PSS	**0.25 mg/mL SWNT**	**0.50 mg/mL SWNT**	**0.80 mg/mL SWNT**
50 bilayers	17,340.3	36,369.7	12,941.4
100 bilayers	15,640.9	5,572.4	3,331.2

Table 3. SWNT-PSS/PVA thin films fabricated with SWNT dispersed in different PSS concentrations (first number denotes strain sensitivity for a testing load rate of 0.10 mm/sec and the second for a load rate of 0.05 mm/sec).

(a)

0.4% PSS	0.25 mg/mL SWNT	0.50 mg/mL SWNT	0.80 mg/mL SWNT
$(SWNT\text{-}PSS/PVA)_{50}$	0.573 / 0.520	0.542 / 0.521	0.653 / 0.272
$(SWNT\text{-}PSS/PVA)_{100}$	0.193 / 0.209	0.199 / 0.309	0.472 / 0.412
$(SWNT\text{-}PSS/PVA)_{200}$	-	0.172 / 0.164	-

(b)

0.7% PSS	0.25 mg/mL SWNT	0.50 mg/mL SWNT	0.80 mg/mL SWNT
$(SWNT\text{-}PSS/PVA)_{50}$	1.016 / 1.397	1.132 / 1.404	1.805 / 1.448
$(SWNT\text{-}PSS/PVA)_{100}$	0.389 / 0.229	0.421 / 0.325	0.808 / 0.483
$(SWNT\text{-}PSS/PVA)_{200}$	-	0.299 / 0.100	-

(c)

1.0% PSS	0.25 mg/mL SWNT	0.50 mg/mL SWNT	0.80 mg/mL SWNT
$(SWNT\text{-}PSS/PVA)_{50}$	1.220 / 1.464	1.293 / 1.531	1.516 / 1.565
$(SWNT\text{-}PSS/PVA)_{100}$	0.915 / 1.066	1.022 / 1.254	1.161 / 1.266
$(SWNT\text{-}PSS/PVA)_{200}$	-	0.813 / 1.250	-

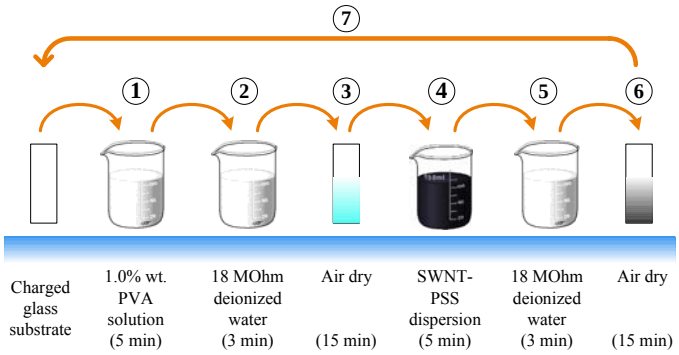

(a)

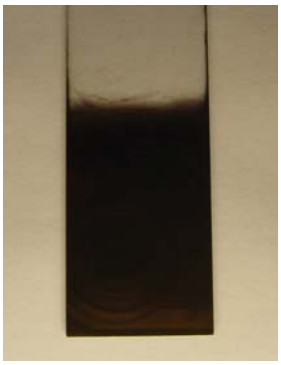

(b)

Figure 1. (a) Illustration of the layer-by-layer process to manufacture conformable SWNT-PE thin films. (b) Final 100-bilayer SWNT-PE thin film on a transparent glass substrate.

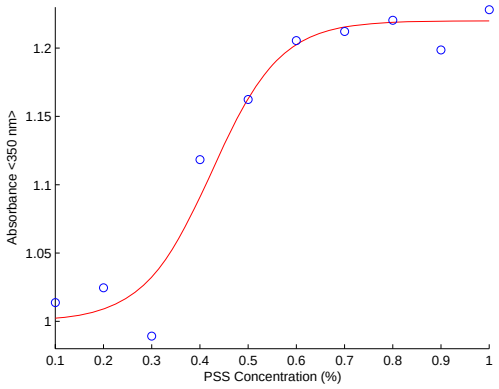

Figure 2. Relative absorption of 350-nm wavelength light for varying SWNT dispersed in increasing concentrations of PSS solution.

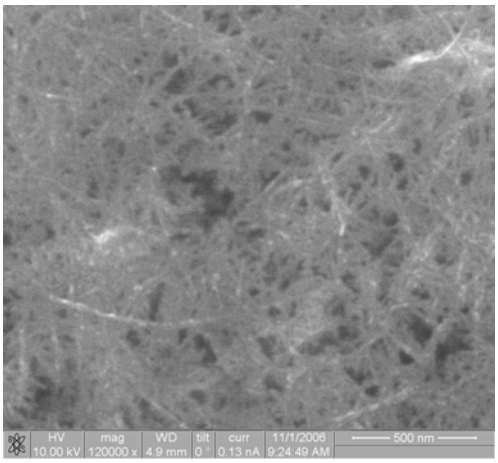

Figure 3. SEM image of 0.80 mg/mL SWNT in 0.7% PSS (SWNT-PSS/PVA)$_{60}$ thin film indicating adequately dispersed SWNT deposited within the bulk composite.

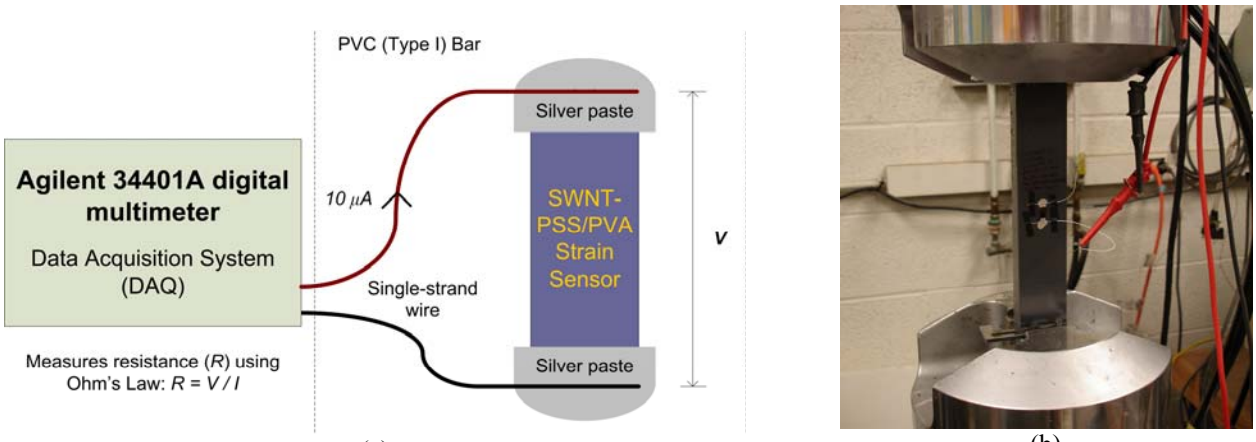

(a) (b)

Figure 4. (a) Schematic showing time-domain sampling of thin film resistance to applied strain. (b) SWNT-PSS/PVA strain sensor epoxy bonded to a PVC specimen and fixed within an MTS-810 load frame.

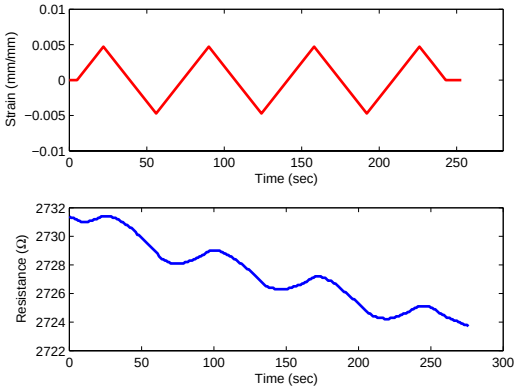

Figure 5. Representative time history response of an (SWNT-PSS/PVA)$_{100}$ thin film (0.7% PSS) (bottom) subjected to a three-cycle tensile-compressive load pattern (0.05 mm/sec) (top).

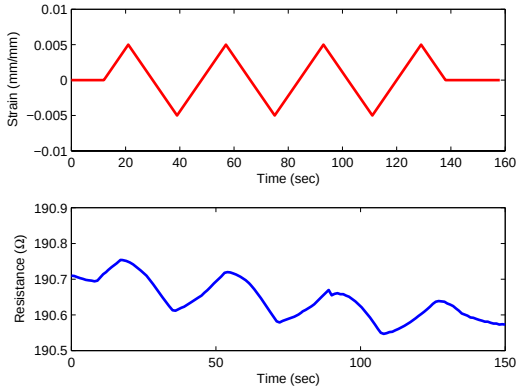

Figure 6. Representative time history response of an $(SWNT\text{-}PSS/PVA)_{100}$ thin film (0.4% PSS) (bottom) subjected to a three-cycle tensile-compressive load pattern (0.10 mm/sec) (top).

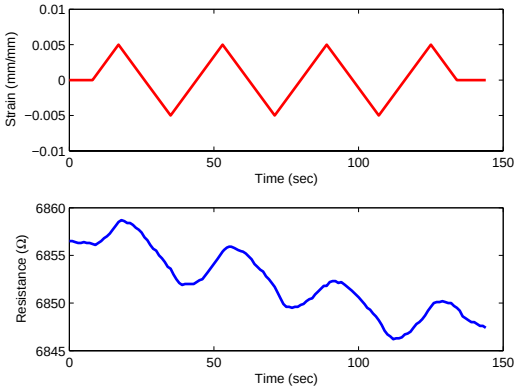

Figure 7. Representative time history response of an $(SWNT\text{-}PSS/PVA)_{50}$ thin film (0.4% PSS) (bottom) subjected to a three-cycle tensile-compressive load pattern (0.10 mm/sec) (top).

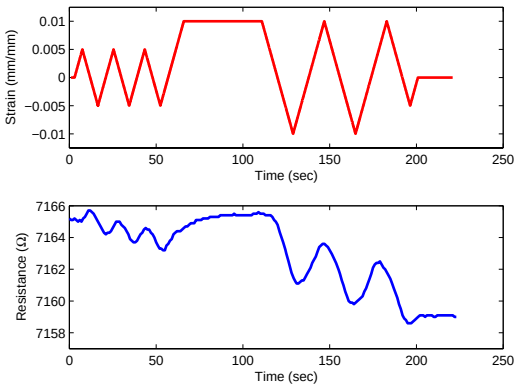

Figure 8. Representative time history response of an $(SWNT\text{-}PSS/PVA)_{100}$ thin film (0.7% PSS) (bottom) subjected to a non-uniform load pattern to ±10,000 μm/m strains (0.10 mm/sec) (top).

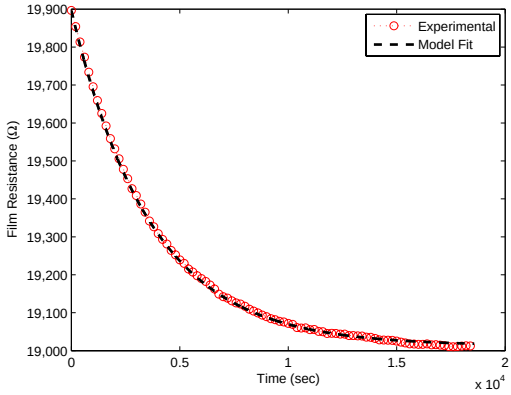

Figure 9. Unloaded (SWNT-PSS/PVA)$_{50}$ thin film's exponential decay in resistance over time.

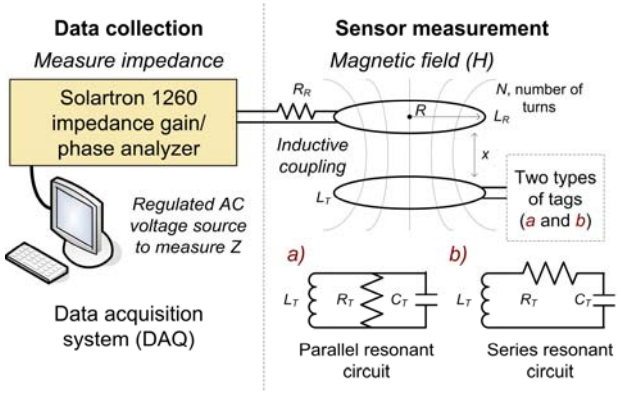

(a)

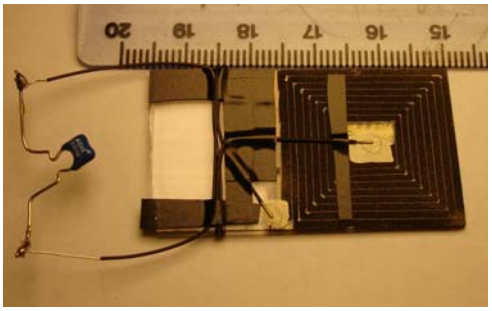

(b)

Figure 10. (a) Schematic showing operating principle of an inductively-coupled RFID system. (b) Patterned SWNT-PSS/PVA thin film for use as an inductively-coupled antenna.

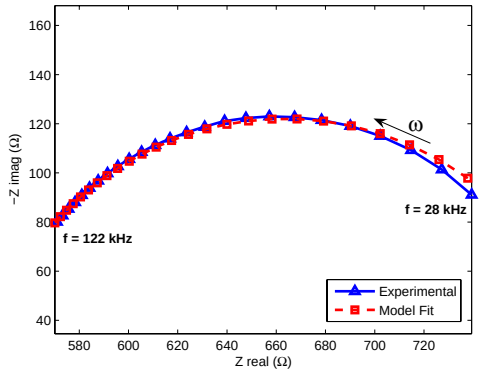

Figure 11. Model-updated fitting of equivalent parallel-RC circuit to EIS experimental data (0.8 mg/mL SWNT in 1.0% PSS v. 1.0% PVA, 50 bilayers).

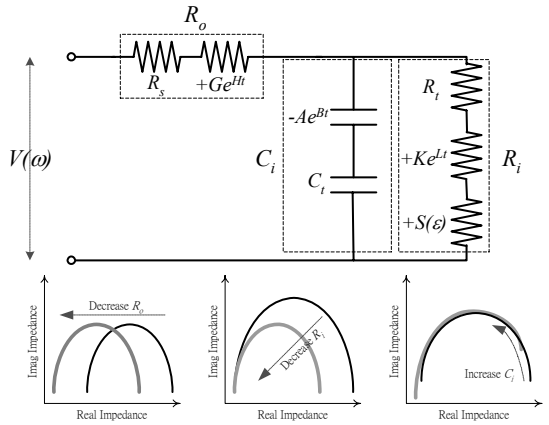

Figure 12. Changes in Cole-Cole plot responses due to variations in equivalent circuit element parameters.

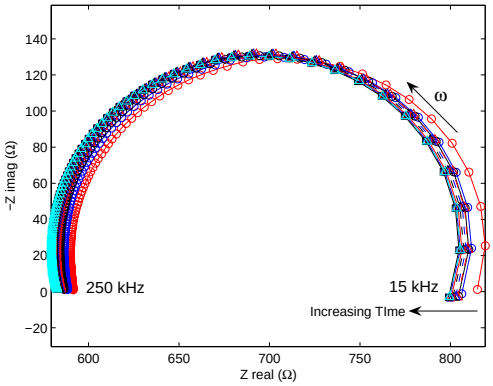

Figure 13. Multiple EIS analyses on an unloaded SWNT-PSS/PVA thin film with increasing time.

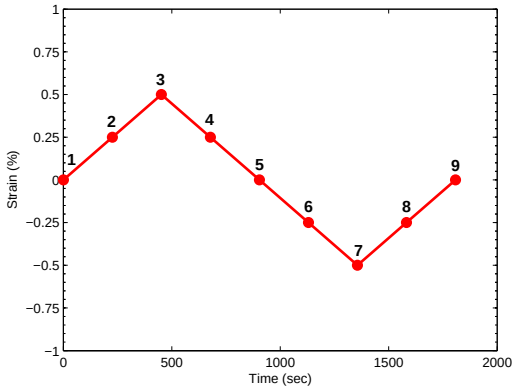

Figure 14. A one-cycle tensile-compressive load pattern applied to SWNT-PSS/PVA specimens for EIS analyses.

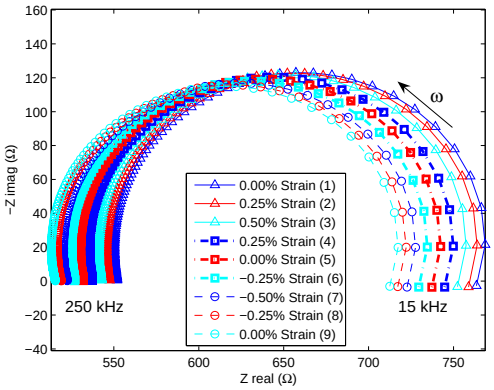

Figure 15. Corresponding EIS response of thin film to tensile-compressive cyclic loading (Figure 14) including the time-exponential-decay of film resistance (Figure 13).

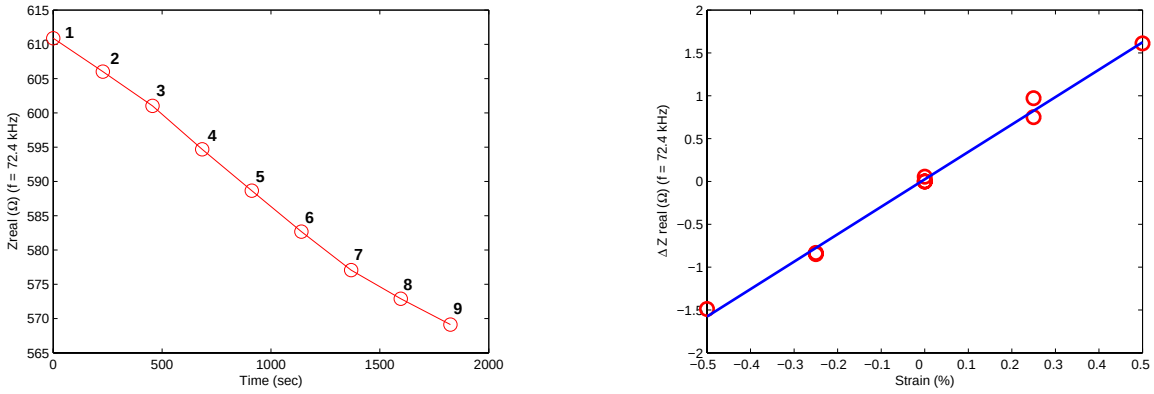

(a) (b)

Figure 16. (a) Impedance-real (Z_{real}) at 72.4 kHz from EIS analyses sampled over time (numbers correspond to series of load tests shown in Figure 14). (b) Relative changes in Z_{real} as a function of applied strain after post-processing to show near-linear SWNT-PSS/PVA piezoresistive response.

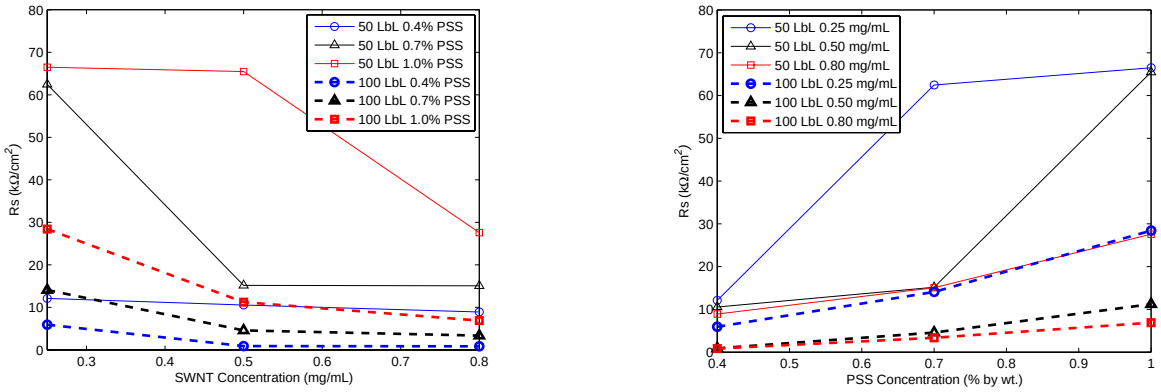

(a) (b)

Figure 17. (a) Series resistor R_s decreases resistance as carbon nanotube concentration is increased (a similar effect is observed for R_t) while PSS concentration is fixed. (b) Plot of R_s showing increasing resistance with greater PSS concentration while SWNT concentration is fixed.

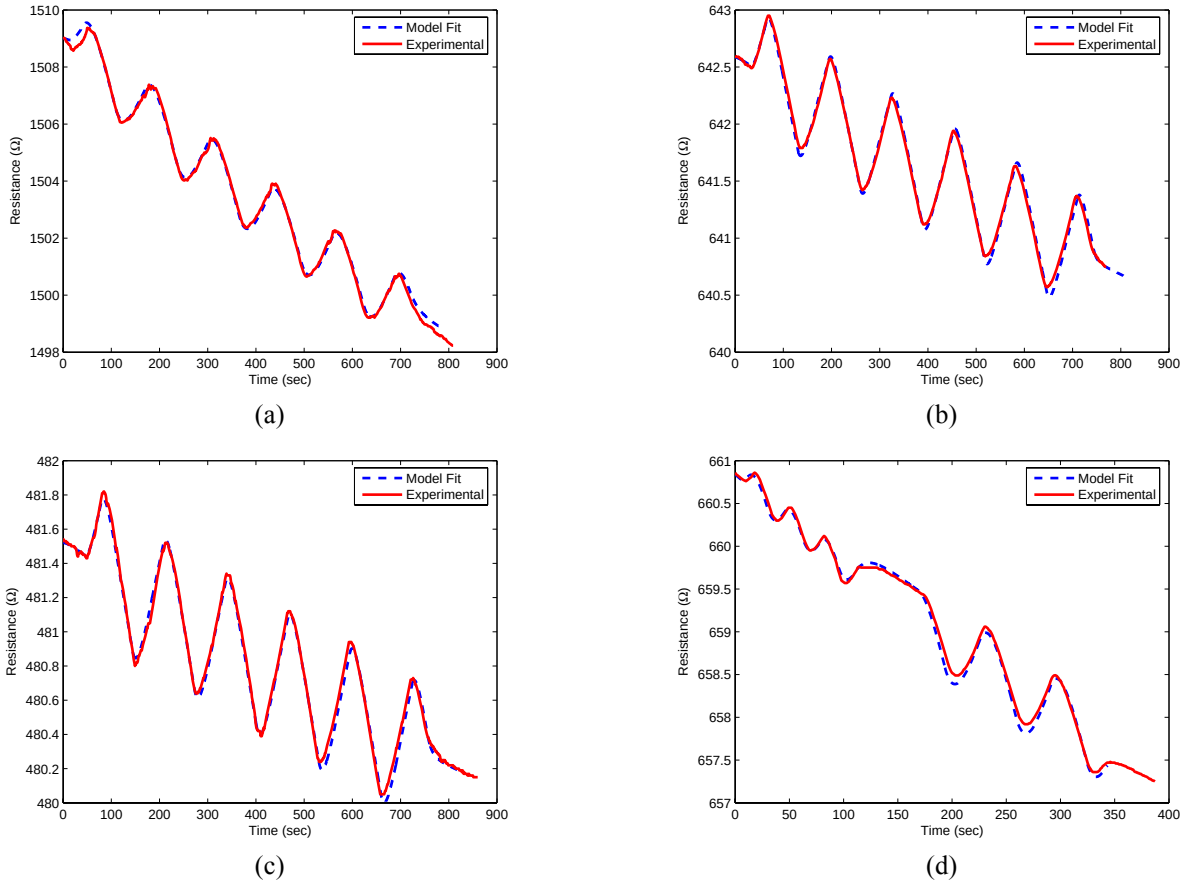

Figure 18. (a) Overlay of RC-parallel circuit model fit and experimental data for 0.50 mg/mL SWNT in 0.4% PSS 100-bilayers thin film under cyclic loading (0.05 mm/sec load rate). (b) 0.80 mg/mL SWNT in 0.4% PSS 50-bilayers thin film cyclically loaded (0.05 mm/sec load rate). (c) 0.80 mg/mL SWNT in 0.4% PSS 100-bilayer thin film cyclically loaded (0.05 mm/sec). (d) Overlay of RC-parallel circuit model fit and experimental data for SWNT-PSS/PVA thin film under non-uniform loading to ±10,000 μm/m strains.

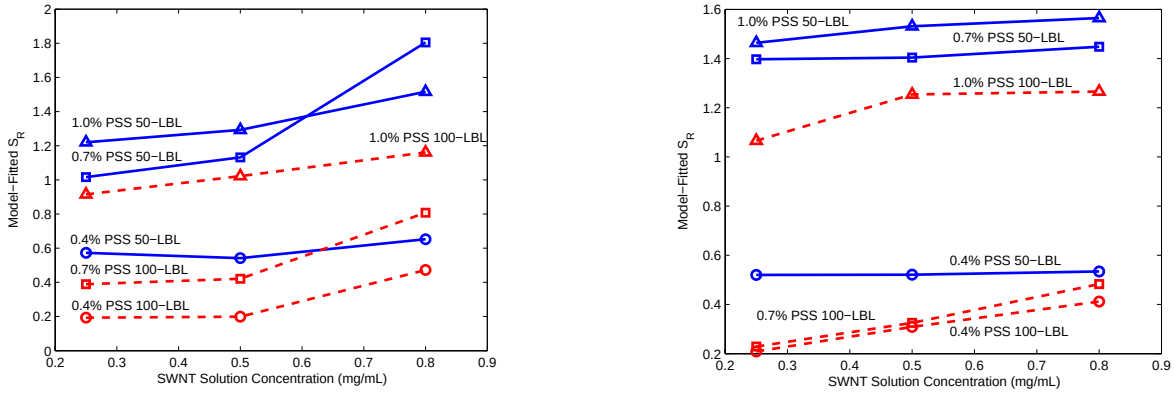

Figure 19. (a) Strain sensitivity for different SWNT-PSS/PVA thin films as a function of dispersed SWNT solution concentration (0.10 mm/sec load rate). (b) 0.50 mm/sec load rate.

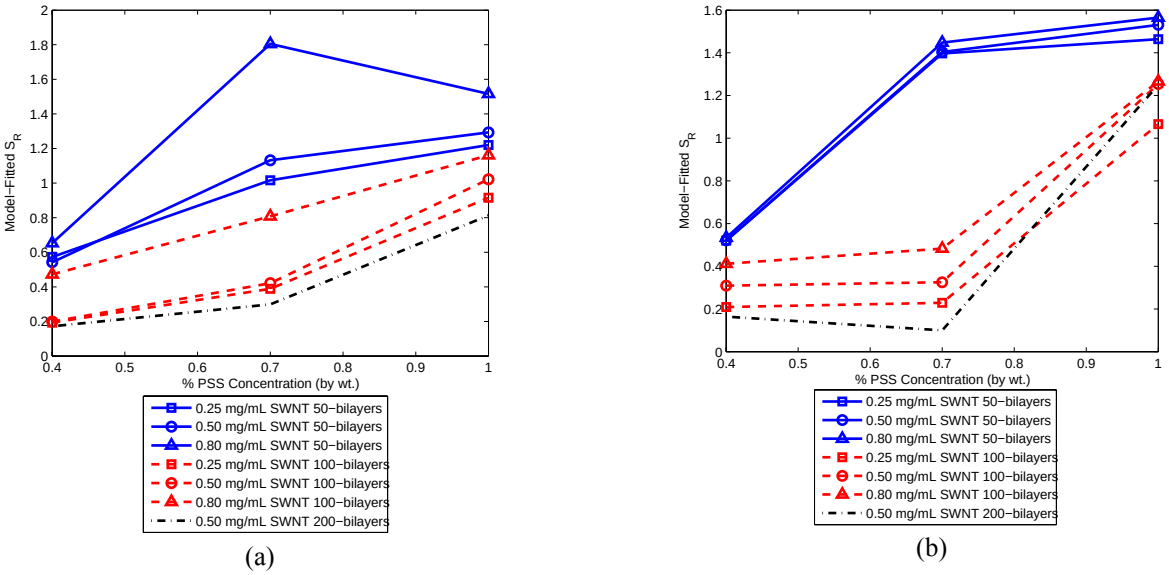

Figure 20. (a) Strain sensitivity for different SWNT-PSS/PVA thin films as a function of PSS concentration (*wt.* %) (0.10 mm/sec load rate). (b) 0.05 mm/sec load rate.

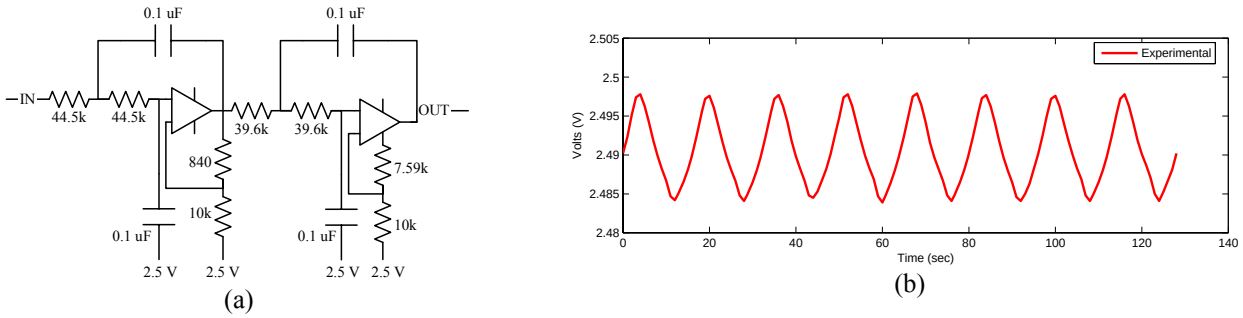

Figure 21. (a) Schematic of the 4-pole low-pass Bessel filter used to filter out low-frequency exponential decay of thin film resistance over time. (b) Band-passed $(SWNT\text{-}PSS/PVA)_{50}$ experimental time history response to applied cyclic tensile-compressive loading to ±5,000 μm/m strains (film is fabricated with 0.80 mg/mL SWNT dispersed in 1.0% PSS).

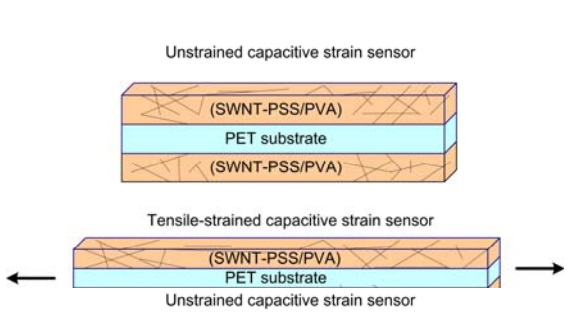

(a)

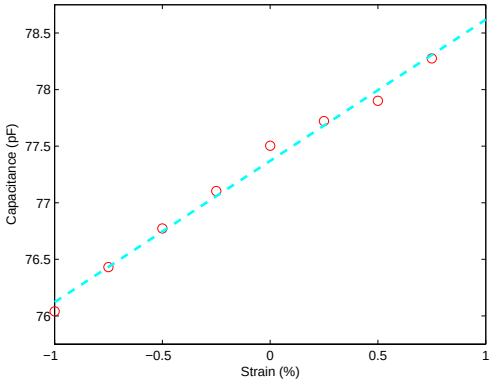

(b)

Figure 22. (a) Schematic illustrating SWNT-on-PET capacitive strain sensor behavior such that PET's Poisson's ratio under applied tension will decrease film width and thickness while increasing length to cause an increase in bandwidth. (b) Preliminary results suggest that when measuring SWNT-on-PET capacitance with applied strain, sensor capacitance will increase linearly with increasingly applied strain.